Draft version February 5, 2008
Preprint typeset using LaTeX style emulateapj v. 10/09/06

arXiv:astro-ph/0612233v1 8 Dec 2006

MONITORING THE BI-DIRECTIONAL RELATIVISTIC JETS OF THE RADIO GALAXY 3C 338

G. Gentile [1], C. Rodríguez [1,2], G. B. Taylor[1,3], G. Giovannini [4,5], S. W. Allen [6], W. M. Lane [7], N. E. Kassim [7]

Draft version February 5, 2008

ABSTRACT

We present the analysis of VLA and VLBA observations of the radio source 3C 338, associated with the cD galaxy NGC 6166, the central dominant galaxy of the cluster Abell 2199. The VLBA observations were done at 8.4 and 15.4 GHz, while the VLA observations were performed at 0.074, 0.330, and 8.4 GHz. The milliarcsecond resolution VLBA data, spanning 7 years, reveal the parsec-scale jets, whose kinematics and orientation cannot be unambiguously derived. Based on the observed morphology, jet/counter-jet length ratio, flux density ratio, and proper motions of the jet components, we consider two possible explanations: either the jets are strongly relativistic and lie within $10^\circ - 20^\circ$ of the plane of the sky, or they are only mildly relativistic, and are pointing at an angle between $30^\circ - 50^\circ$ from the plane of the sky. The arcsecond resolution VLA data enable us to investigate the large scale structure of the radio source. The morphology of the low frequency radio lobes clearly indicates that they are associated with the cavities present in the X-ray emission. Low frequency observations also reveal an extension to the south corresponding to an X-ray hole. The age of these bubbles, computed from the sound speed, the buoyancy time and the radiative age are all in fair agreement with each other. Estimates of the power necessary to inflate these cavities suggest that the accretion power onto the central engine has not been constant over time.

Subject headings: galaxies: active — galaxies: individual (3C 338) — galaxies: jets — radio continuum: galaxies

1. INTRODUCTION

The cD galaxy NGC 6166 is the central dominant galaxy in the nearby ($z = 0.0304$) cluster Abell 2199. This galaxy hosts the relatively powerful radio source, 3C 338, which emits a total power at 330 MHz of 4.4×10^{25} W Hz^{-1}. This radio source has been known for a few decades to have an unusual structure on both large and small scales (e.g. Feretti et al. 1993, Giovannini et al. 1998).

On parsec scales 3C 338 has a compact radio core with two short ($\sim$ 10 pc), symmetric jets. Such highly symmetric jets are rare among 3C (Third Cambridge catalog - Bennett 1962) radio galaxies, though the few that are known (Hydra A - Taylor 1996; PKS 2322−12 - Taylor et al. 1999) are also at the centers of large clusters, suggesting perhaps that the jets in such sources are decelerated on scales of a few parsecs. Here we present Very Long Baseline Array (VLBA) [8] observations from six epochs of monitoring 3C 338 at 8.4 GHz. Three epochs have also been obtained at 15 GHz. These observations are used to study the motions of the inner bidirectional jets in 3C 338.

On kiloparsec scales 3C 338 has two symmetric extended radio lobes, characterized by a steep spectrum ($\alpha \sim -1.7$), and misaligned with the central emission. The two radio lobes are connected by a bright filamentary structure. Polarimetric observations by Ge & Owen (1994) revealed strong rotation measure gradients across most of the extended emission and inferred the presence of cluster magnetic fields. Both the steep radio spectrum and strong filamentary emission may be the result of interactions with the dense intracluster medium. Further evidence of interaction has been reported in X-rays where *ROSAT* and *Chandra* data (Owen & Eilek 1998 and Johnstone et al. 2002 respectively) have shown that the core of the cluster is far from being simple and spherically symmetric. Johnstone et al. (2002) found evidence for temperature and metallicity gradients and for structures in the X-ray gas associated with the radio source. Using new *Chandra* data, Sanders & Fabian (2006) found an approximately circular X-ray surface brightness discontinuity at $\sim$ 55 kpc from the center of the cluster, which they interpret as a weak isothermal shock that might be an important energy transport mechanism. Here we present new 74 and 330 MHz VLA observations, highlighting the existence of large-scale, diffuse emission connected to the X-ray emitting gas.

Throughout this discussion, we assume H_0=70 km s^{-1} Mpc^{-1}, $\Omega_m = 0.3$, $\Omega_\Lambda = 0.7$, and 1 mas = 0.6 pc.

2. OBSERVATIONS AND DATA REDUCTION

The 74 and 330 MHz observations were performed on April 16, 2002 at the VLA in the A configuration.

[1] Department of Physics and Astronomy, University of New Mexico, Albuquerque, NM 87131, USA
[2] Department of Physics, Universidad Simon Bolivar, Sartenejas, Venezuela
[3] National Radio Astronomy Observatory, Socorro NM 87801, USA
[4] Dipartimento di Astronomia, Universita' di Bologna, 40127 Bologna, Italy
[5] Istituto di Radioastronomia - INAF, 40129 Bologna, Italy
[6] Kavli Institute for Particle Astrophysics and Cosmology, Stanford University, Stanford, CA 94305-4060, USA
[7] Naval Research Lab, Code 7213, Washington, DC, 20375, USA
[8] The Very Long Baseline Array (VLBA) and the Very Large Array (VLA) are operated by the National Radio Astronomy Observatory (NRAO), which is a facility of the National Science Foundation operated under cooperative agreement by Associated Universities, Inc.

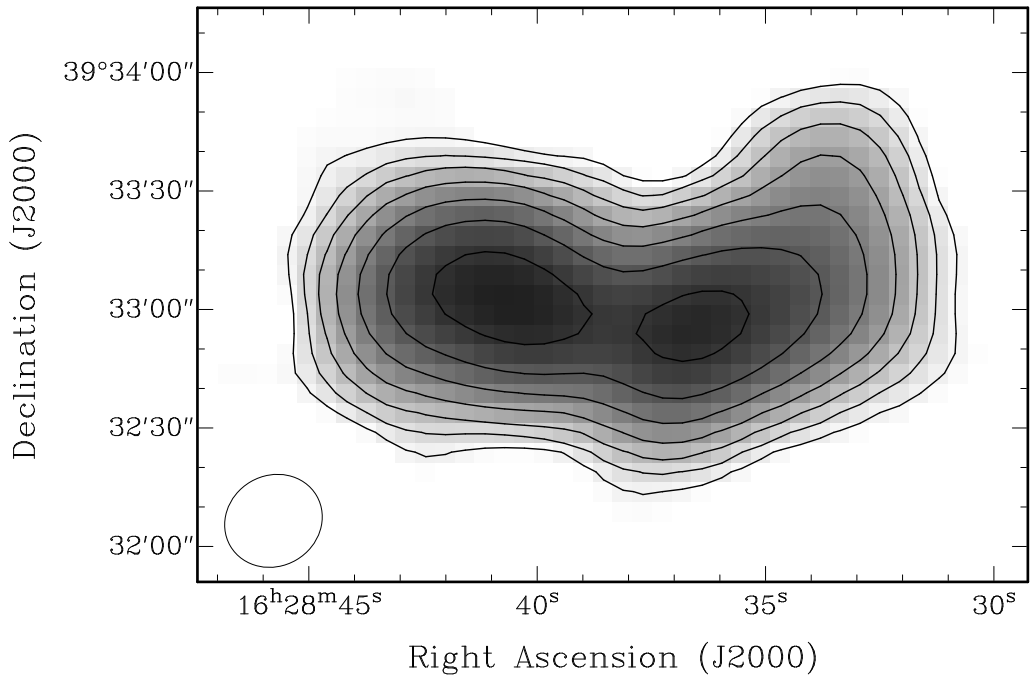

FIG. 1.— Contours of the 74 MHz map of 3C 338. The synthesised beam is shown in the bottom left corner; its FWHM size is 25.3″×22.9″in PA -60°. Contour levels are 0.35 (5σ), 0.7, 1.4, 2.8, 5.6, ... Jy beam^{-1}. The peak flux is 32.7 Jy/beam.

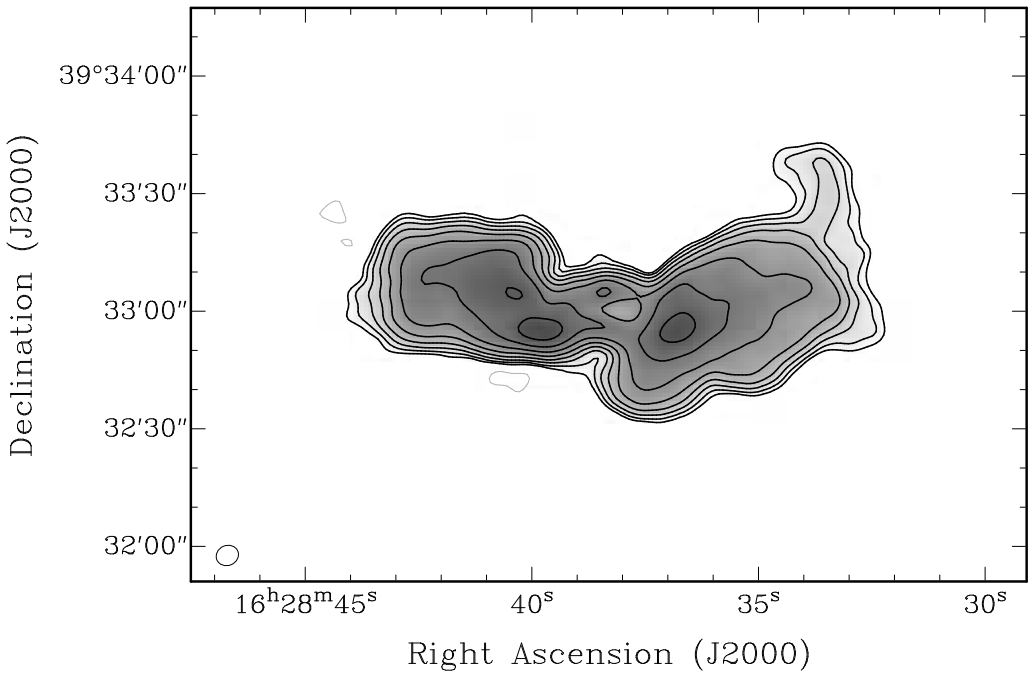

FIG. 2.— Contours of the 330 MHz map of 3C 338. The synthesised beam is shown in the bottom left corner; its FWHM size is 5.8″×5.1″in PA -67°. Contour levels are -5 (grey contours), 5 (4.5σ), 10, 20, 40, 80, ... mJy beam^{-1}. The peak flux is 0.9 Jy/beam.

At both frequencies the source was observed in spectral line mode in order to permit removal of narrow-band radio frequency interference (RFI), which at those frequencies severely affects the data, as well as to mitigate the effects of bandwidth smearing. Primary calibration and bandpass corrections for the 330 MHz and 74 MHz data were made using short observations of 3C286 and 3C405 respectively. The data were edited for radio frequency interference and averaged in frequency to reduce the number of channels. Phases from several observations of 3C286 were transferred to the 330 MHz data to provide an initial calibration, while the final 330 MHz image was used as a model to estimate inital phase calibration for the 74 MHz data. Both datasets were further processed using several iterative loops of imaging and phase self-calibration followed by two loops of imaging and amplitude self-calibration with the standard AIPS tasks IMAGR and CALIB. Although 3C338 dominates its field, imaging was done using multiple facets in a wide-field mode at both frequencies for increased model accuracy during the final amplitude self-calibrations.

At low radio frequencies, the ionosphere can introduce a refractive phase error that causes a gross position offset in an image. This cannot be removed via the self-calibration process because the phase error is common to all antennas. As a result, small angular offsets are typical in low-frequency maps processed by this method. When absolute coordinate accuracy is important it is standard practice to remove the offset by registering point sources in the image to known coordinates. For these data we removed a roughly 10" shift by comparing the field sources to the NVSS catalog.

Data reduction was also performed using AIPS for the 8.4 GHz VLA observations in the A, B, CnB, and C configurations. The data were taken over the course of five epochs: 1994 Nov. 17, 1995 Sept. 11, 1998 Dec 02, 2000 Feb. 26, and 2001 Jun 01 (See Table 1). Standard calibration procedures were performed, as well as imaging and self-calibration. Once all the data were properly calibrated and the final images obtained for each epoch were satisfactory, all the visibilities from the five epochs were combined using the task DBCON.

The 8.4 GHz and 15.4 GHz VLBI observations were carried out over the course of six epochs, performed on 1994 Nov. 17, 1995 Sept. 11, 1997 Sept. 26, 1998 Dec 02, 2000 Feb. 26, and 2001 Jun 01 (see Table 2). Observations in 1994, and 1995, were obtained using all ten elements of the VLBA and a single VLA antenna. Observations in 1997 onwards were taken using a global array of between 12 and 15 antennas. Both right and left circular polarizations were recorded using 2 bit sampling across a bandwidth of 8-16 MHz. The VLBA correlator produced 16 frequency channels across each 8 MHz IF during every 2 s integration.

Parallactic angle effects resulting from the altitude-azimuth antenna mounts were removed using the AIPS task CLCOR. Amplitude calibration for each antenna was derived from measurements of antenna gain and system temperatures during each run. Delays between the stations' clocks were determined from a short observation of the bright calibrator 3C 279 using the AIPS task FRING (Schwab & Cotton 1983). Calibration was applied by splitting the multi-source data set immediately prior to preliminary editing, imaging, deconvolution, and self-calibration in Difmap (Pearson et al. 1994). Multiple iterations of phase self-calibration and imaging were applied to each source (including calibrators and 3C 338) before any attempt at amplitude self-calibration was made. The preliminary models developed in Difmap were subsequently applied in AIPS to refine the gain corrections, to determine the leakage terms between the RCP and LCP feeds (using the unpolarized calibrator OQ 208) and to correct for residual phase differences between polarizations. Final imaging and self-calibration were performed in Difmap.

No polarized flux has been detected from 3C 338 at either 8.4 or 15.4 GHz in epochs 2000 or 2001 in which careful polarization calibration was performed. Typical 2σ limits on the linearly polarized flux density are <70 μJy at 8.4 GHz and <200 μJy at 15.4 GHz. This corresponds to a limit of $< 0.4\%$ for the jet component E2. The low polarization is consistent with the high rotation measure expected for an orientation of the inner radio jets close to the plane of the sky (Zavala & Taylor 2002).

3. RESULTS

3.1. *VLA Images*

The low frequency maps are shown in Figures 1 and 2. The emission at those frequencies is more extended than the higher frequency maps presented in Giovannini et al. (1998) and Johnstone et al. (2002), especially in the western lobe, even though the comparison at 74 MHz is difficult due to the relatively poor angular resolution. An example of a new feature in the 330 MHz, compared to the higher frequency maps, is the plume extending northwards from the northern tip of the western lobe; this feature evident, but somewhat smeared out at 74 MHz. The source total flux is reported in Table 1. We estimated also the flux density for the west lobe (67.7 Jy at 74 MHz and 10.3 Jy at 330 MHz) and for the east lobe (76.2 Jy at 74 MHz and 11.3 Jy at 330 MHz) by integrating over regions defined by the lobe shapes; since the core is relatively weak at those frequencies, it is not crucial to select carefully the regions over which the integration has to be done.

Figure 3 shows the VLA image at 8.4 GHz and resolution of $1.4''$, from A, B, BnC, and C configurations, obtained by combining the visibilities from the five epochs; the map was deconvolved using a multi-resolution CLEAN (Wakker & Schwarz 1988), to highlight both the small-scale and the large-scale structures. This algorithm is a variant of the standard CLEAN (Högbom 1974), which uses Gaussian components of different sizes; in our case we used components with sizes up to $16''$. The total flux in this map is 157.8 mJy, with a peak of 86.1 mJy beam^{-1}. The west and east lobe flux density is respectively 44 mJy, and 43 mJy; the difference with respect to the total flux density is due to the core and central jet region. The structure observed in 3C 338 is similar to the one obtained by Ge & Owen (1994) at 5 GHz, with two diametrically opposed jets, as well as a peculiar ridge connecting the eastern and western lobes of emission. The orientation and position of this image is consistent with our VLA images at 74 and 330 MHz. The optical center of the cluster consists of four components (A, B, C, and D, Minkowski 1961; Burbidge 1962), the brightest of which corresponds to the core of the radio emission (Burns et al. 1983; Fanti et

TABLE 1
VLA Observations of 3C 338.

Date	Frequency (GHz)	Configuration	Core flux density (mJy)	rms (mJy/beam)	Total Flux (mJy)	VLBI total* (%)	Peak Flux mJy
2002 Apr 12	0.074	A	...	70	140900	...	32700
2002 Apr 12	0.330	A	...	1.1	21600	...	900
1994 Nov 17	8.4	C	85	0.018	143	103	85
1995 Sep 11	8.4	A	88	0.027	103	98	88
1998 Dec 02	8.4	C	80	0.033	142	99	80
2000 Feb 26	8.4	B	82	0.026	132	110	82
2001 Jun 01	8.4	BnC	91	0.016	158	95	91

* The VLBI total was obtained dividing the total cleaned flux in the VLBI observations at 8.4 GHz (see Table 2) by the VLA peak flux at 8.4 GHz

TABLE 2
VLBI Observational Parameters for 3C 338 *.

Date	Frequency (GHz)	Bandwidth (MHz)	Antenna	Scan min	Time hours	Peak mJy	rms mJy/beam	Total Cleaned Flux (mJy)
1994 Nov 17	8.4	15	VLBA+Y1	60	7.1	29	0.101	88
1995 Sep 11	8.4	14	VLBA+Y1	60	7.1	22	0.088	87
1997 Sep 26	8.4	28	VLBA+Y1+EB	60	9.9	18	0.033	72
1998 Dec 02	8.4	32	Global [1]	24	4.8	21	0.029	79
	15.4	32	VLBA+Y27+EB	24	4.7	18	0.114	50
2000 Feb 26	8.4	32	Global [2]	20	5.0	27	0.037	91
	15.4	32	VLBA+Y27+EB	20	4.0	25	0.133	71
2001 Jun 01	8.4	32	Global [3]	30	5.0	37	0.045	86
	15.4	32	VLBA+Y27+EB	30	5.5	22	0.114	51

* Global = VLBA + EB, MC, WB, GO, RO, Y27. Telescope Codes: VLBA= Very Long Baseline Array, VLA = Very Large Array, Y1 = single VLA antenna, Y27 = 27 VLA antennas, EB = Effelsberg, MC = Medicina, WB = Westerbork, GO = Goldstone, RO = Robledo.[1] GO, RO, and WB were out, as well as the VLBA antenna in Saint Croix.[2] GO, and RO were out, as well as the VLBA antenna in Hancock.[3] WB was out.

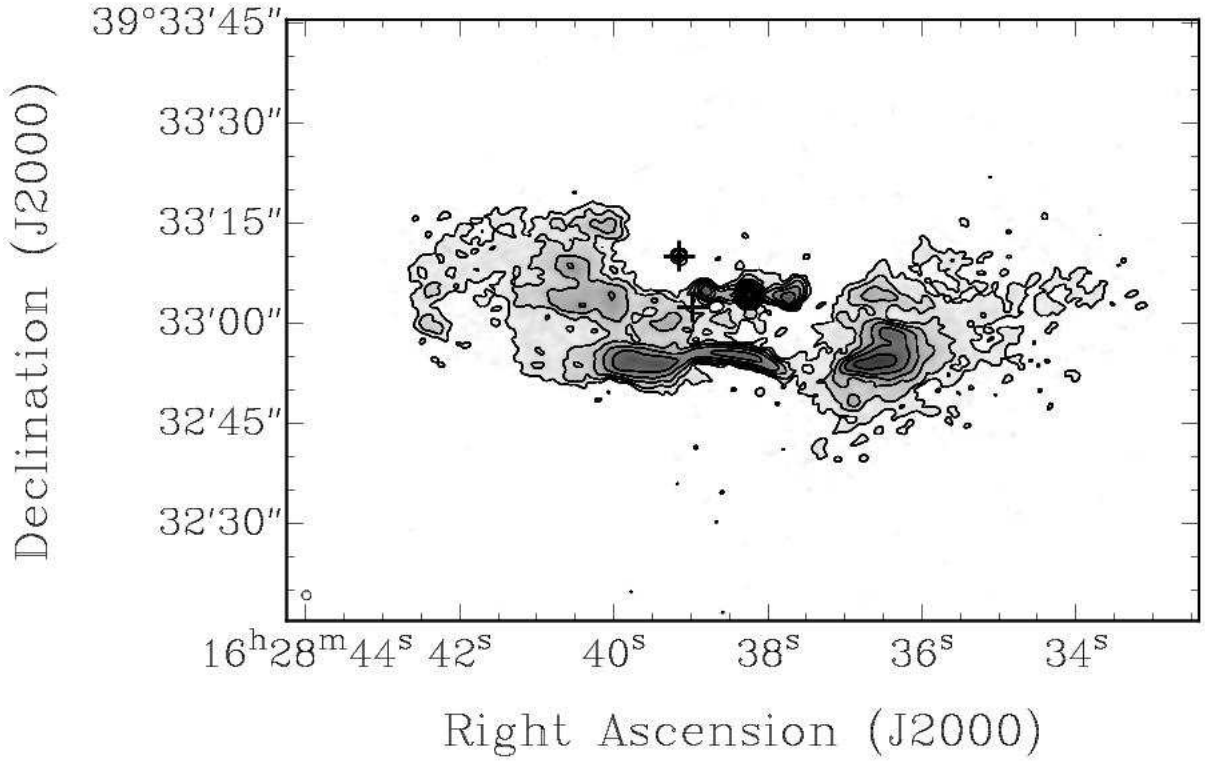

Fig. 3.— Contours of the 8.4 GHz map of 3C 338 from the VLA A, B, BnC, and C configurations at 1.4″ resolution. The synthesised beam is shown in the bottom left corner. Contours levels are 32 (4σ), 64, 128, 256, ... μJy beam^{-1}. The crosses indicate the location of component B (north) and C (south); see Section 3.1.

al. 1986). Recent HST observations (Martel et al. 1999, Capetti et al. 2000) have found the second and third brightest components (B and C) to be elliptical galaxies at similar projected distances from NGC 6166. Their positions are indicated in Figure 3. Ge & Owen (1994) identified a weak feature found in their 5 GHz maps, to the northeast of the radio core, as optical component B. This component is also present in our 8.4 GHz map, with a peak flux of 0.15 mJy beam^{-1}.

3.2. *VLBI Images*

Figure 4 shows "naturally" weighted 8.4 and 15.4 GHz images from the VLBI 2000 observations. "Natural" weighting does not correct for the local density of samples in the (u, v) plane and thus gives a lower resolution. Both images were tapered and restored with a circular 2 mas synthesized beam. The orientation of our VLBI images is consistent with the orientation observed in our VLA images at 0.074, 0.330, and 8.4 GHz. VLBI observations recover 95% or more of the VLA core flux density at 8.4 GHz (Table 1). In 2000 the VLBI total is 10% higher than the VLA, indicating a calibration error of $\sim 10\%$ in one or both data sets.

In Figure 5, which shows the 8.4 GHz 1997 and 2001 epochs at full resolution of 1.4×0.6 mas (PA 0°), we see a bright central component, which we designated C, as well as two jets to the east and west respectively. We designated the brightest component in the eastern jet as E2, and the brightest component in the western jet as W2.

Motion and variability studies were performed by fitting six elliptical or circular Gaussian components in Difmap to the 2000 self-calibrated visibility data at 8.4 GHz. Then, this model was used to fit the data corresponding to 1994, 1995, 1997, 1998, and 2001 epochs at the same frequency. We let only position and flux density vary, in order to fit the independently self-calibrated visbility data, while all the other parameters were held fixed at the 2000 values. Results from our fits are listed in Table 3. Since phase-referencing was not performed, all positions are relative positions only. We selected the strong compact, VLBI core (component C) as the reference. Statistical errors in the positions range from 0.02 to 0.06 mas and are derived from the component size divided by the signal-to-noise ratio.

We obtained an estimate for the sizes of C, E2, and W2 based on our 8.4 GHz model fits (see Table 3), finding that they are all compact with sizes smaller than 0.58 mas or 0.36 pc. To fit the data two more components were necessary: component E1 (extended and diffuse at large distance from component C) to recover the extended jet flux density and component E3 to fit the jet in between components C and E2.

A new component (E4) was found in the 2001 VLBI observations at 8.4 GHz. This component is at ~ 0.4 mas east from component C and is almost twice as large as it, implying that new jet components are still being ejected from the core. This component is however always visible in 15 GHz images and probably not seen in 1998 and 2000 data at 8.4 GHz because of its more limited angular resolution.

For the model-fitting we used the 8.4 GHz data instead of those at 15 GHz (shown in Figure 6) because in the latter the noise is 3 times higher while the components are half the flux density. Hence, despite their higher resolution, the 15 GHz data provide weaker constraints; however the model-fitting performed on the 15 GHz shows the same trend as the 8.4 GHz data.

3.3. *Motions and Variability*

We do not discuss components E1 and E3 since these two last components are extended and diffuse and do not correspond to well defined structure. Component E4 is present in only one epoch at 8.4 GHz, but it is visible in all epochs at 15 GHz with no appreciable proper motion.

To calculate the relative velocity of the components, we chose component C as the reference. We were able to compare the relative motions of both E2 and W2 by fitting a line to each component's projected separation, derived from the Gaussian modelfitting, as a function of time. The results obtained are shown in Table 4 and plotted in Figure 7. Component E2 is moving away from component C to the east, while component W2 is moving away from it to the west.

Significant motion with respect to component C was obtained for both E2 and W2, yielding a value of 0.055 ± 0.005 mas/y or (0.112 ± 0.010)c and 0.115 ± 0.008 mas/y or (0.234 ± 0.016)c respectively.

To study component variability in 3C 338, we compared the flux density for components C, E2, and W2 over each of our six epochs at 8.4 GHz. Errors for each region were calculated based on the rms noise and our estimated absolute flux calibration errors ($\sim 5\%$). The resulting fractional variation light curves are shown in Figure 8. We also added the core's VLA flux density light curve found from the five epochs studied at 8.4 GHz. Errors for this region were based on our estimated absolute flux calibration errors ($\sim 3\%$). These light curves were created by dividing each region's flux density at each epoch by the flux density measured in the first epoch. The light curves for components E2 and W2, and the core's VLA flux density are displaced on the y-axis by 1, 2, and 3 units, respectively.

From Figure 8 it can be noted that from 1994 to 1995 the displayed light curves for components C, E2, and W2 decreased in flux density, independently of the subsequent evolution. This leads us to believe that there was an error of about 30% in the calibration of the 1994 data. Component C substantially increases in flux, going from 16 mJy in 1995 to 33 mJy in 2001. Component E2, on the other hand, decreases in flux density, going from 16 mJy in 1995 to 4 mJy in 2001. Finally, component W2 is less monotonic, since it increases in flux density from 1995 to 1997 (going from 5 mJy to 8 mJy), and then it decreases from 1997 to 2001 (going from 8 mJy to 4 mJy). Finally, we find that there is no significant variation in the VLA core flux density light curve over the 7 yr baseline. This lack of variability was unexpected from previous observations (Giovannini et al. 1998), since the arcsecond core flux density was a factor $\sim 1.5 - 2$ higher in 1990-1991. However, more recent 8 GHz VLA data from 2005 (Partridge & Lin, priv. comm.) indicate a core flux density of 84 mJy, consistent with the very small variations found in $1994 - 2001$. It appears that the core has been in a quiescent phase since 1994.

3.4. *Spectral Index Distribution*

TABLE 3
GAUSSIAN MODEL COMPONENTS*.

Component	Epoch	S (Jy)	r (mas)	θ (^{o})	a (mas)	b/a	Φ (^{o})	χ^2
C...	1994.877	0.022 ± 0.001	0.00	0.0	0.29	1.00	2.9	1.03
	1995.693	0.016 ± 0.001	0.00	0.0	0.29	1.00	2.9	0.14
	1997.741	0.018 ± 0.001	0.00	0.0	0.29	1.00	2.9	1.86
	1998.916	0.022 ± 0.001	0.00	0.0	0.29	1.00	2.9	1.49
	2000.151	0.029 ± 0.002	0.00	0.0	0.29	1.00	2.9	1.13
	2001.415	0.033 ± 0.002	0.00	0.0	0.29	1.00	2.9	1.17
E1...	1994.877	0.012 ± 0.001	12.47	88.1	19.46	0.14	277.4	1.03
	1995.693	0.015 ± 0.001	11.36	86.9	19.46	0.14	277.4	0.14
	1997.741	0.012 ± 0.001	12.96	87.7	19.46	0.14	277.4	1.86
	1998.916	0.013 ± 0.001	13.64	87.5	19.46	0.14	277.4	1.49
	2000.151	0.016 ± 0.001	13.51	88.3	19.46	0.14	277.4	1.13
	2001.415	0.010 ± 0.001	12.59	86.7	19.46	0.14	277.4	1.17
E2...	1994.877	0.023 ± 0.001	1.48	83.7	0.80	0.33	298.1	1.03
	1995.693	0.016 ± 0.001	1.54	85.5	0.80	0.33	298.1	0.14
	1997.741	0.012 ± 0.001	1.60	85.8	0.80	0.33	298.1	1.86
	1998.916	0.010 ± 0.001	1.71	81.8	0.80	0.33	298.1	1.49
	2000.151	0.008 ± 0.001	1.76	84.9	0.80	0.33	298.1	1.13
	2001.415	0.0040 ± 0.0002	1.92	89.7	0.80	0.33	298.1	1.17
E3...	1994.877	0.018 ± 0.001	1.03	81.7	5.33	0.06	80.3	1.03
	1995.693	0.027 ± 0.002	0.63	72.0	5.33	0.06	80.3	0.14
	1997.741	0.019 ± 0.001	1.60	82.6	5.33	0.06	80.3	1.86
	1998.916	0.022 ± 0.001	1.35	88.3	5.33	0.06	80.3	1.49
	2000.151	0.026 ± 0.001	1.23	80.7	5.33	0.06	80.3	1.13
	2001.415	0.023 ± 0.001	1.63	82.0	5.33	0.06	80.3	1.17
E4	2001.415	0.009 ± 0.001	0.38	80.1	0.48	1.00	353.3	1.17
W1...	1994.877	0.008 ± 0.001	8.85	271.2	18.39	0.13	275.6	1.03
	1995.693	0.008 ± 0.001	6.05	266.2	18.39	0.13	275.6	0.14
	1997.741	0.0050 ± 0.0003	8.31	269.8	18.39	0.13	275.6	1.86
	1998.916	0.0070 ± 0.0004	7.81	268.4	18.39	0.13	275.6	1.49
	2000.151	0.009 ± 0.001	6.88	268.7	18.39	0.13	275.6	1.13
	2001.415	0.0030 ± 0.0002	10.08	266.7	18.39	0.13	275.6	1.17
W2...	1994.877	0.007 ± 0.001	1.25	255.6	0.85	0.47	53.1	1.03
	1995.693	0.0050 ± 0.0003	1.30	255.1	0.85	0.47	53.1	0.14
	1997.741	0.0080 ± 0.0004	1.48	260.5	0.85	0.47	53.1	1.86
	1998.916	0.0050 ± 0.0003	1.71	261.0	0.85	0.47	53.1	1.49
	2000.151	0.0040 ± 0.0002	1.82	254.7	0.85	0.47	53.1	1.13
	2001.415	0.0040 ± 0.0003	1.99	259.1	0.85	0.47	53.1	1.17

* NOTE - Parameters of each Gaussian component of the model brightness distribution are as follows: Component, Gaussian component; Epoch, year of observation (see Table 2); S, flux density; r, θ, polar coordinates of the center of the component relative to the center of component C ; a, semimajor axis; b/a, axial ratio; Φ, component orientation; χ^2, goodness-of-fit for six component model in each epoch. All angles are measured from north through east. Errors in flux are based on our absolute amplitude calibration as well as the rms noise. See text for a discussion of the position errors.

TABLE 4
COMPONENT MOTION FITTING RESULTS.

Component	Velocity (mas/y)	Velocity (c)	Angle of Motion * (^{o})
C	Reference Component	...	...
E2	0.055 ± 0.005	0.112 ± 0.010	90.84
W2	0.115 ± 0.008	0.234 ± 0.016	264.44

* Angles measured from north through east.

The 1998 VLBI images at 8.4 and 15.4 GHz were matched in resolution in order to obtain a spectral index distribution across the source (Figure 9). This epoch was chosen based on the quality of the data, number of antennas out during observations, and noise in the final image. Table 5 lists the flux densities measured from the matching resolution images, as well as the spectral index obtained for components C, E2, and W2. A steep spectrum was found for both the eastern and western jets, obtaining a spectral index equal to −0.95 for E2, and −0.71 for W2. The region near E2 and W2 components appears flatter than connecting regions. The very inverted (red in Figure 9) regions could suggest the presence of a jet structure or are probably due to the different uv-coverage between the two data sets. Component C has a flatter spectral index of -0.11, indicating that it is associated with the center of activity (see Table 5)

At arcsecond resolution we did not derive a spectral index image because of the low resolution of VLA 74

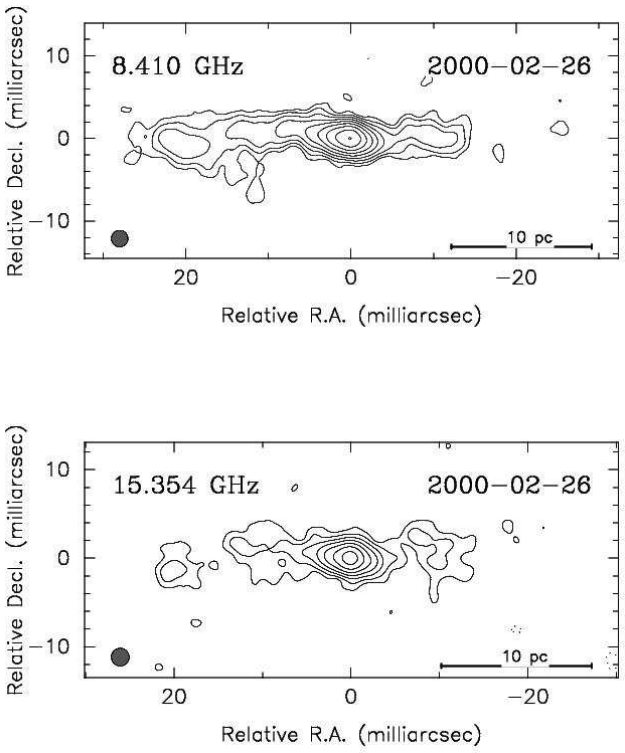

FIG. 4.— Contemporaneous VLBA observations of 3C 338 at 8 and 15 GHz from the 2000 epoch. Both images have been tapered and restored with a circular 2 mas synthesized beam (drawn in the lower left-hand corner each plot). Contours are drawn logarithmically at factor 2 intervals with the first contour at 0.15, and 0.4 mJy/beam at 8 and 15 GHz respectively.

MHz data. The integral spectral index for the two lobes is α_{330}^{74} = -1.26 and $\alpha_{8.4}^{0.3}$ = -1.68 for the west lobe and α_{330}^{74} = -1.28 and $\alpha_{8.4}^{0.3}$ = -1.72 in agreement with previous results (Burns et al. 1983).

4. DISCUSSION

4.1. *Kinematics in 3C 338 and Evolution of Jet Components*

The symmetric source structure on the parsec scale suggests an orientation near to the plane of the sky. However the jet length and total flux density (see Figs. 5 and 6) and the asymmetric E4 component suggests that the east side is the approaching one. Therefore we will consider in the next discussion the east jet as the main jet and the west one as the counter-jet.

4.1.1. *Jet orientation and bulk velocity of 3C 338 on the parsec scale*

In the simple beaming model for simultaneously ejected jet components moving in opposite directions, either the arm length ratio D or the flux density ratio R can be used as a first constraint on the intrinsic speed $\beta = v/c$ and the angle of the jets to the line of sight θ (Taylor & Vermeulen 1997). The arm length ratio, D, is given by

$$D = \frac{d_E}{d_W} = \left(\frac{1+\beta\cos\theta}{1-\beta\cos\theta}\right), \qquad (1)$$

where the apparent projected distances from C (assumed for the moment to be the origin of the jet) are d_E for the eastern jet (approaching side) and d_W for the western jet (receding side).

We applied this relation to the whole parsec scale structure visible in the 8.4 GHz images (e.g. Fig. 4a, top) and we measured an arm ratio ~ 1.87 corresponding to $\beta\cos\theta \sim 0.30$. Alternatively we could consider the distance from the core of components E2 and W2 but because of different proper motion velocity we have an arm length ratio from 1.18 (1994 epoch)to 0.96 (2001 epoch).

Similarly, the flux density ratio, R, between the eastern and western jet is

$$R = \frac{S_E}{S_W} = \left(\frac{1+\beta\cos\theta}{1-\beta\cos\theta}\right)^{k-\alpha} \qquad (2)$$

where α is the spectral index, $k = 2$ for a continuous jet, and $k = 3$ for discrete jet components (e.g. Lind & Blandford 1985).

The flux density ratio was obtained dividing the sum of the fluxes of component E2 over the six epochs by the sum of the fluxes of component W2 over the six epochs (see Table 3), yielding a value of $R = S_E/S_W = 2.21 \pm 0.33$. From this result we can obtain a value for $\beta\cos\theta$. Using $k = 2$ and the mean spectral index between E2 and W2, $\alpha = -0.83 \pm 0.06$, we obtained $\beta\cos\theta = 0.14 \pm 0.04$

If we consider component E4 and assume that the symmetric W4 component is missing because of relativistic effects on a symmetric emission, we derive a brightness ratio R > 12 corresponding to $\beta\cos\theta > 0.46$.

4.1.2. *Jet orientation and velocity of 3C 338 on the parsec scale from proper motion measures*

We can also constrain the jet orientation and velocity (pattern velocity) by comparing different epoch data and measuring the proper motion of jet substructures.

In Figure 7 we plot the positions of the two strongest jet components, E2 and W2, derived from the modelfitting. These inner jet components both appear fairly straight to within the errors in the measurements: there is no clear sign of acceleration or deceleration. Given these motions and the symmetry of the source (Figures 4 and 5), it is reasonable to assert that E2 and W2 were ejected at the same time. Deep observations at 8.4 GHz reveal that there is continuous emission from the core outwards. The jet is probably not made up of discrete blobs that can be well described by elliptical Gaussian components that we identify and modelfit. Rather the jet appears to be a continuous flow, with features of enhanced emission (possibly shocks) that propagate down the jet.

Using the values obtained for the velocities of components E2 and W2 (see Table 4), and using the distance from these components to component C (see Table 3) we calculated the velocity ratio obtaining $\mu_E/\mu_W = 0.478 \pm 0.077$ and $d_E/d_W = 0.965 \pm 0.001$ respectively.

In this case the approaching side of the jet is moving slower than the receding side. This result either i) implies that the measured proper motion is not a real motion but is due to variability of jet brightness or ii) requires that the real core is moving to the west.

The first case has been discussed in many sources where apparent motion with different velocities as well as fixed structures have been found as in M87 (see e.g.

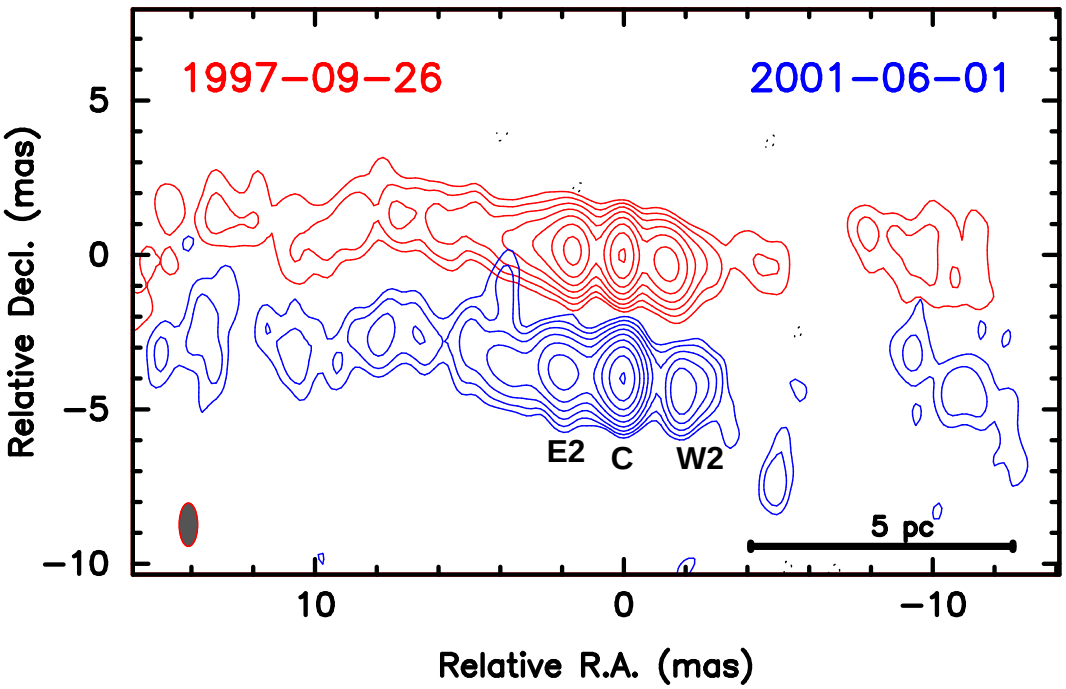

FIG. 5.— An overlay at 8.4 GHz of the 1997 (in red) and 2001 (in blue) VLBA observations at full resolution of 1.4 × 0.6 mas in position angle 0°. Contours are drawn starting at 0.13 mJy/beam for both epochs and increase by factors of two thereafter.

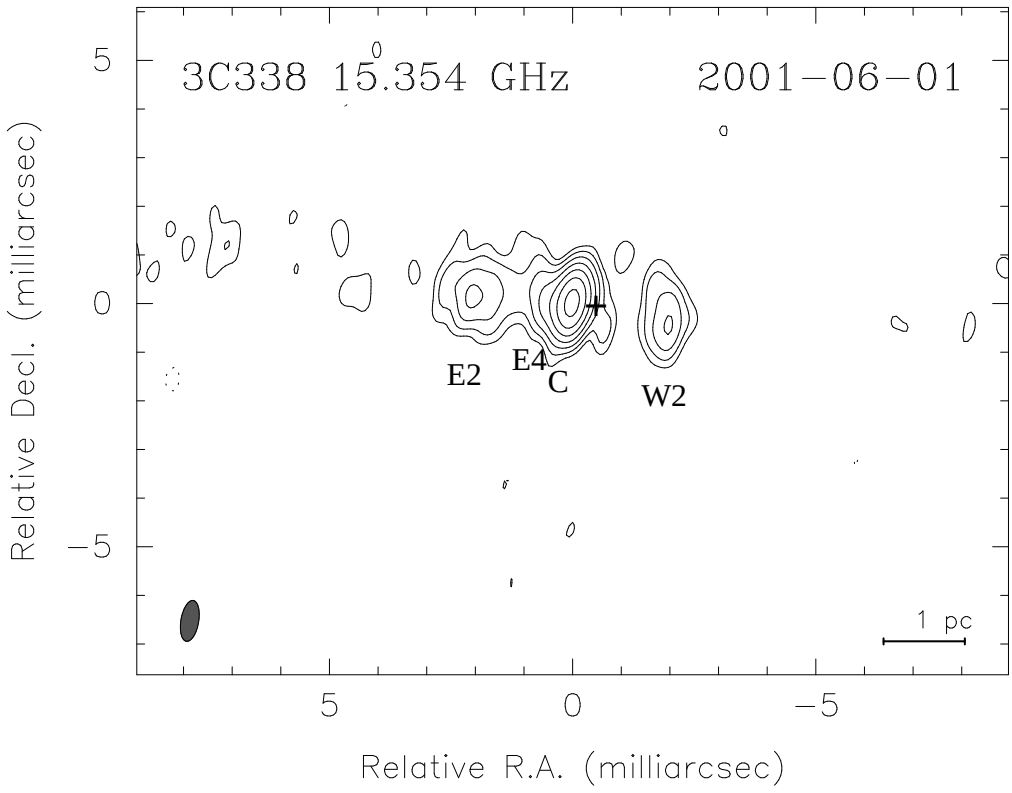

FIG. 6.— 15 GHz VLBI map at full resolution, using natural weighting. Contours start at 2.5×10^{-4} mJy beam^{-1}. The beam is 0.85 × 0.37 mas in position angle -9.7°. The components fitted from the 8 GHz data are shown; the cross indicates the position of the origin of the jets in our model.

Dodson et al. 2006 and references therein), and Markarian 501 (Giroletti et al. 2004).

In the second case by assigning a velocity to component C we can make the velocity and arm length ratio consistent with the assertion that E2 and W2 were ejected at the same time, that is, we can make these two ratios equal. Under this assumption we obtain that component C is moving to the east at $\mu_c = 0.058$c. With this value we then determined the velocity of both E2 and W2 with respect to component C and finally estimate their age to be 23 yr, meaning that they were ejected roughly in 1978. This implies a total displacement of component C of 0.63 mas, or about one beam FWHM. The true core could still be unseen if its flux is smaller than about 4% of the peak flux of C, or about 1 mJy/beam. We expect that in a few more years the core (which should be stationary) should become apparent, if this model is correct. Component C is required to be intrinsically brigther on one side, i.e. its corresponding component west of the true core is required to be suppressed.

Another independent constraint on the two parameters β and θ can be obtained from the separation rate $\mu_{sep} = |\mu_E| + |\mu_W|$, which is not subject to the uncertainty in the reference point. From geometry and the conversion of angular to linear velocity we have

$$v_{sep} = \mu_{sep} D_a (1+z) = \frac{2\ \beta\ c \sin\theta}{(1-\beta^2 \cos^2\theta)}, \qquad (3)$$

where v_{sep} is the projected separation velocity, D_a is the angular size distance to the source, and z is the redshift. Using the values obtained for the motion of components E2 and W2, we obtained a projected velocity separation equal to $v_{sep} = (0.346 \pm 0.026)c$.

4.1.3. *Jet kinematics and orientation*

Observational results discussed above do not present strong constraints on the jet kinematics and orientation for this symmetric source. We have two different possible explanations for the parsec scale jet structure in 3C 338:

1) Jets on the parsec scale are only mildly relativistic and the pattern velocity from the proper motion is indicative of the real jet velocity. In this case the 3C 338 nuclear source is moving as discussed above, and this could be in agreement with the nuclear dynamics of this complex cD galaxy where we have 4 different optical nuclei: a strong evidence that this galaxy suffered many major mergers and that the central region is not yet relaxed.

Figure 10 shows the jet velocity (β) plotted against the inclination of the source (θ). The intersection obtained by plotting the results for $\beta cos\theta$ and v_{sep} gives us constrains for both values β and θ. For $\beta cos\theta = 0.14$ and $v_{sep} = 0.34$, we obtain $\theta = (50 \pm 11)^\circ$ and $\beta = 0.22 \pm 0.04$. Note, however, that a fully consistent picture of the orientation and kinematics of 3C 338 is difficult to obtain: using as a first constraint the arm length ratio would lead to slightly lower values of β and higher values of θ.

2) We can assume instead that parsec scale jets are highly relativistic. This is supported by previous results on low power radio galaxies (see e.g. Giovannini et al. 2001) and on BL Lac sources (Giroletti et al. 2006) which according to unified models should be the beamed population of FR I radio galaxies. In this case the pattern velocity (proper motion of components E2 and W2) is not related to the jet bulk velocity and these structures (such as component E4) are standing shocks as found in other sources (see discussion above). Unfortunately we cannot use the core dominance to derive constraints since the core showed a strong variability and there is clear indication of a restarted activity. In this last case indeed the core power is not related to the extended emission which originated in previous active regime. From the jet/counter-jet ratio and the arm length ratio assuming a jet moving with Lorenz Factor Γ in the range 3 to 10 (see Giovannini et al. 2001) the orientation angle should be in the range 70° – 80° from the line of sight.

4.2. *Jet Power in 3C 338*

X-ray studies have shown that the black holes at the centers of galaxies, groups, and clusters are capable of inflating cavities or 'bubbles' in the surrounding X-ray emitting gas (e.g. Fabian *et al.* 2003, 2005 ; Bîrzan *et al.* 2004 ; Forman *et al.* 2005).

Figure 11 shows an X-ray image overlayed with the contours of the 330 MHz radio map (Figure 2). The core of the radio emission in 3C 338, though barely distinguishable at 330 MHz, is clearly identifyable with the highest X-ray brightness region and therefore with the center of the cluster. Similar to many recent examples in the literature, the correspondence between the location of the radio lobes and X-ray cavities (Johnstone et al. 2002) suggests an expansion of the former into the surrounding X-ray emitting gas.

We estimated the energy required to inflate the large scale bubbles in 3C 338, based on the results presented by Allen et al. (2006); they studied the properties of the bubbles inflated by the inner lobes, which are still attached to the jets (see their Fig. 3) and thus likely to still be subjected to inflation. At a projected distance of $\sim$ 20 kpc from the core, the electron density is ~ 0.02 cm^{-3} and the temperature is $kT \sim 3$ keV. With these values we were able to calculate the thermal pressure, P, of the surrounding X-ray emitting gas. The energy E required to create the observed bubbles in the X-ray emitting gas (e.g. Allen et al. 2006) is approximately:

$$E \sim 4PV, \qquad (4)$$

where V is the volume of the cavity. We have modelled the bubbles as ellipsoids with volumes $V = 4\pi r_l r_w^2/3$, where r_1 is the semi-axis length along the jet direction, and r_w is the semi-axis width across it. Using the 330 MHz image (see Figure 2) as a guide to estimate r_l and r_w, we estimate energies require to inflate the large-scale cavities of $E \sim 2.5 \times 10^{59}$ erg and $E \sim 3.7 \times 10^{59}$ erg for the eastern and western large-scale lobes, respectively. These values are $\sim$ 300 times larger than the one obtained by Allen et al. (2006) for the inner bubbles.

For a comparison, assuming equipartition conditions with the ratio between electrons and protons k = 1 and a filling factor $\phi = 1$ we find in the same volume a minimum energy $\sim 3 \times 10^{58}$ erg and a magnetic field $H_{eq} \sim 15\ \mu$G.

We also estimated the age of the bubbles as (see e.g. Bîrzan *et al.* 2004)

$$t_{age} = R/c_s, \qquad (5)$$

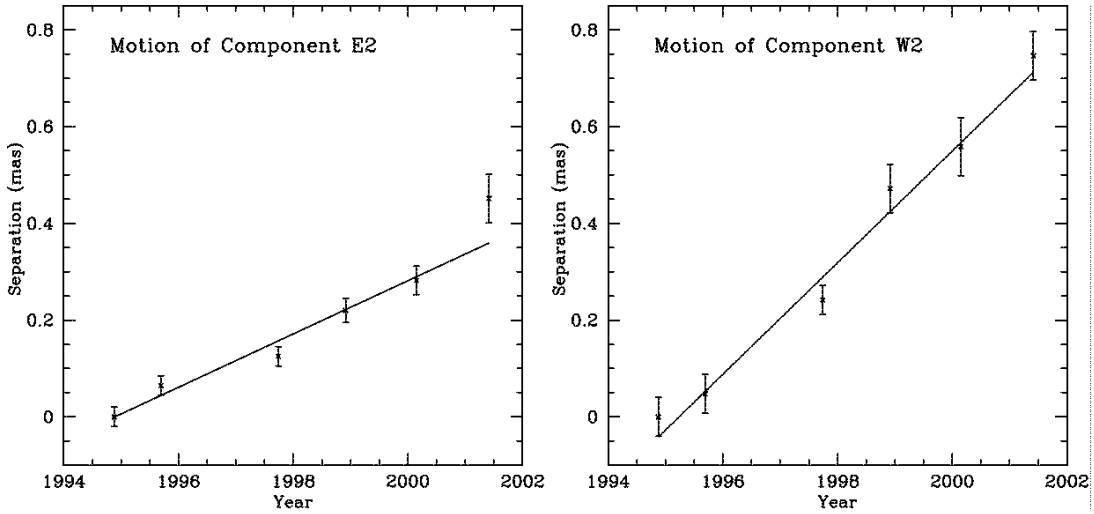

FIG. 7.— Velocities of the components E2 and W2 derived from the straight line which best fits the measured positions from the 8.4 GHz data only (see Fig. 3). The zero point is taken to be the position of the component at the first epoch. See text for a discussion of the position errors.

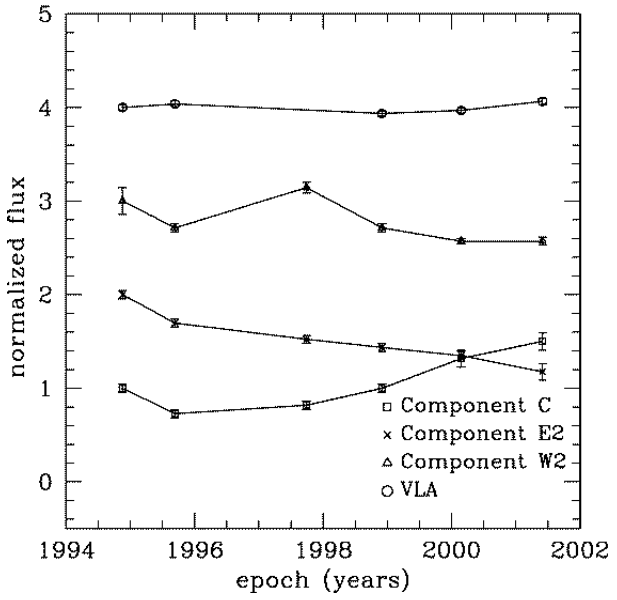

FIG. 8.— Light curves of the three brightest components of 3C 338: C, E2, and W2, as well as the total VLA flux density. The values used to produce this graph were taken from Tables 3 (for C, E2, and W2) and 1 (for the core's VLA peak flux) and are discussed in §3.3. The displayed light curves were created by dividing each region's flux at each epoch by the first epoch's flux of each region respectively. The light curves of component E2, component W2, and the core's VLA peak flux are displaced on the y-axis by 1, 2, and 3 units respectively. Errors are estimated from the rms noise and the absoulute flux calibration errors for each epoch.

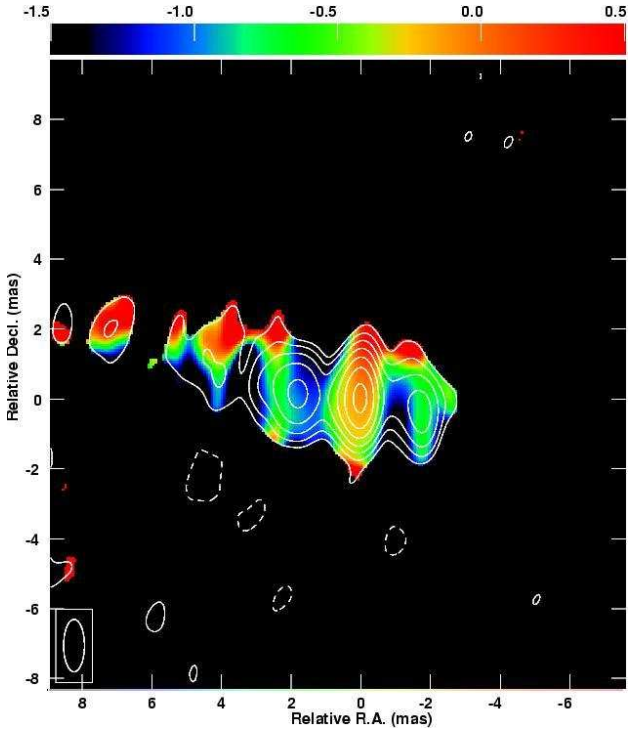

FIG. 9.— Spectral index distribution between 8.4 and 15.4 GHz from the 1998 observations. The contours are taken from the 15.4 GHz observations and are set at 3σ, increasing by a factor of 2 thereafter.

where R is the distance of the bubble center from the black hole, and c_s is the adiabatic sound speed of the gas at the bubble radius. Using R estimated from our 330 MHz image ($\sim$ 20 kpc for both bubbles), we obtain $t_{age} \sim 2.2 \times 10^7$ yr, in good agreement with the radiative age estimated assuming equipartition conditions ($\sim 4 \times 10^7$ yrs). Finally, the power involved in 'blowing' the bubbles can be estimated from

$$P_{jet} = E/t_{age}. \quad (6)$$

Using our values obtained for E and t_{age} we get $P_{jet} \sim 4.3 \times 10^{44}$ erg s^{-1}.

Another estimate can be given using the buoyancy time t_{buoy} instead of t_{age}, as the bubbles might have separated from the AGN. It can be calculated from the buoyancy velocity $v_{\rm b} = \sqrt{2gV/SC_{\rm D}}$, where $g = GM(< R)/R^2$ is the gravitational acceleration at radius R (the distance between the cluster core and the bubble center), V is the volume, $S = \pi r_{\rm w}^2$ is the area of the bubble in the rise direction, and $C_{\rm D}$ is the drag coefficient, whose value is ~ 0.75. Then, the buoyancy time can be computed from $t_{buoy} = R/v_{\rm b}$. We find $t_{buoy} = 2.4 \times 10^7$ yr for the east bubble and $t_{buoy} = 2.1 \times 10^7$ for the west bubble, values which are very similar to t_{age}. Using t_{buoy} we get $P_{jet} \sim 4.0 \times 10^{43}$ erg s^{-1} and $P_{jet} \sim 4.7 \times 10^{44}$ erg s^{-1} for the eastern and western outer bubbles. Allen et al.

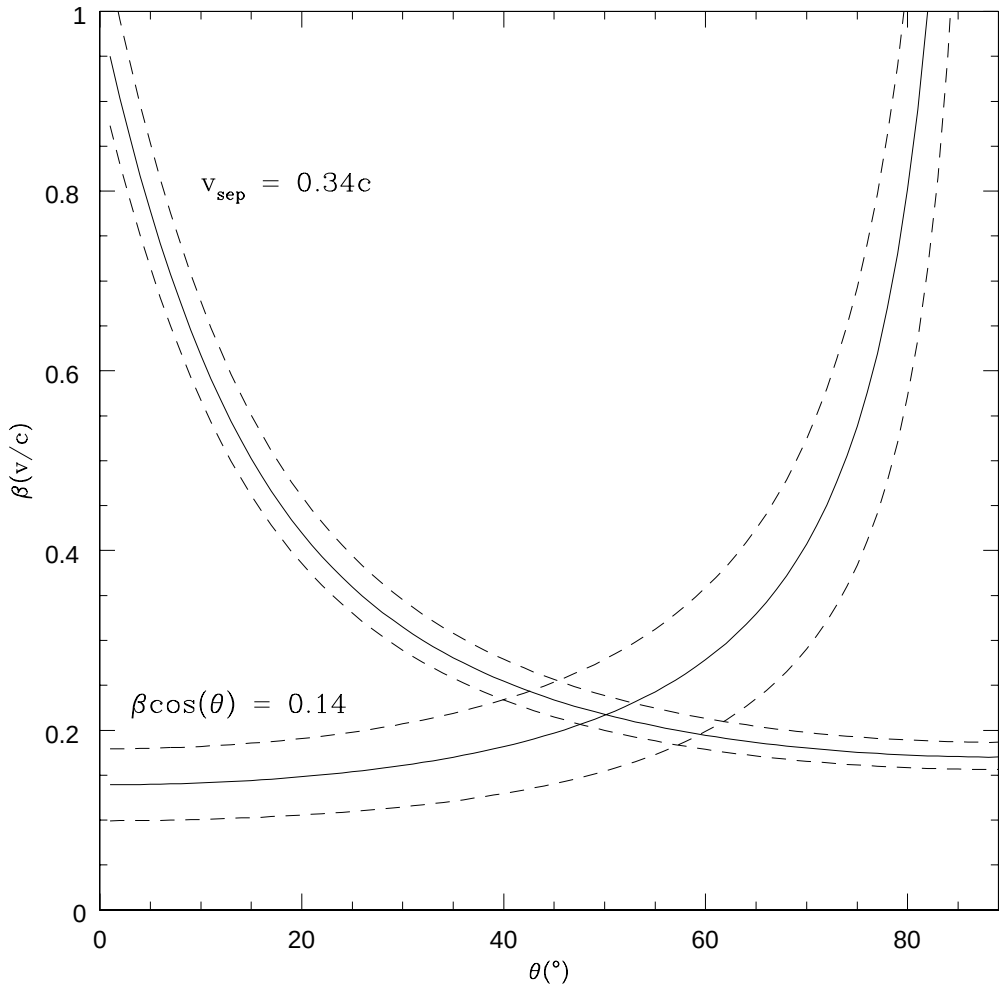

FIG. 10.— The jet velocity (β) plotted against the inclination of the source (θ) measured from the line of sight to the jet axis. The solid increasing line represent the constraint $\beta\cos\theta = 0.14 \pm 0.04$ from the flux ratio of components E2 and W2. The solid decreasing line shows the constraint from the observed separation velocity, $h^{-1}v_{sep}$, for E2 and W2 with $h = 0.71 \pm 0.05$ where $h = H_0/100$ km s^{-1} Mpc^{-1}. The dashed lines represent the uncertainties.

(2006) obtained a value of $P_{jet} = (0.741 \pm 0.316) \times 10^{43}$ erg s^{-1} for the inner bubble, which is ~ 60 times smaller than the value that we obtain for the large scale bubble. Allen et al. (2006) also calculated the accretion power, obtaining $P_{Bondi} = (3.06^{+3.65}_{-1.36}) \times 10^{43}$ erg s^{-1}. The fact that the current value for the accretion power is smaller than the power necessary to inflate the older, large-scale bubble suggests that the accretion rate or accretion mode has varied with time. We also compared our results for E and P_{jet} with those obtained by Dunn & Fabian (2004) for the large scale bubbles and verified that they show good agreement. Minor differences are due to slightly different conventions adopted in the two studies.

TABLE 5
CONTINUUM SPECTRUM RESULTS*.

Component	Frequency (GHz)	Flux (mJ)	α_{8-15}
C...	8.4	20.98 ± 1.08	−0.11 ± 0.01
	15.4	19.61 ± 1.09	
E2...	8.4	8.07 ± 0.43	−0.95 ± 0.04
	15.4	4.55 ± 0.34	
W2...	8.4	3.97 ± 0.23	−0.71 ± 0.07
	15.4	2.59 ± 0.24	

* Results obtained from the 1998 observations. The flux densities were measured from matching resolution images.

5. CONCLUSIONS

We analysed VLA and VLBA observations of the radio source 3C 338, associated with the cD galaxy NGC 6166, the central dominant galaxy of the galaxy cluster Abell 2199. The VLBA observations probe the innermost region close to the jet with a resolution of the order of 1 pc. The VLA observations, performed at 0.074, 0.330, and 8.4 GHz, trace the large-scale emission from the radio lobes out to $40 - 50$ kpc.

The VLBA data reveal the pc-scale jets, whose kinematics and orientation we did not manage to derive in an unambiguous way. The observations suggest two possible explanations: either the jets are strongly relativistic and the jets lie within $10°-20°$of the plane of the sky, or they are only mildly relativistic, and they are pointing at an angle of $30°-50°$.

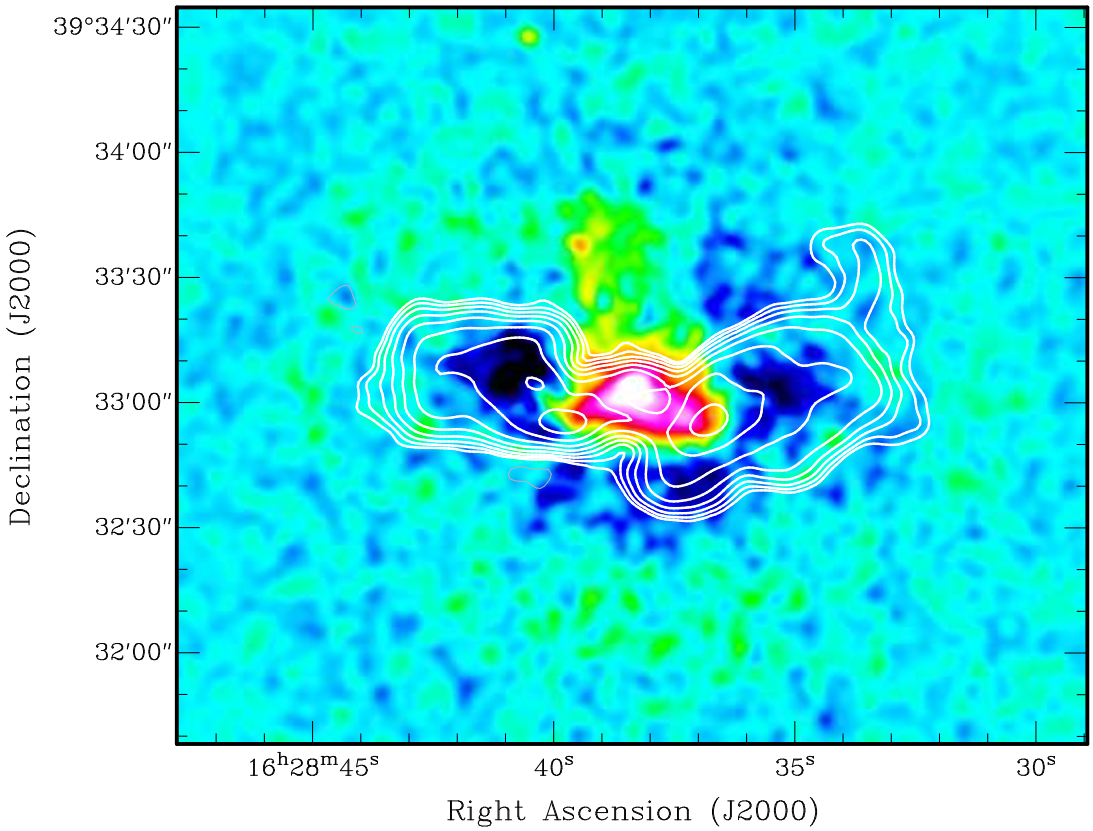

FIG. 11.— Unsharped-masked Chandra X-ray image in the 0.5-8.0 keV band (colours), formed from the difference of raw images smoothed with Gaussian kernels of width $\sigma = 3$ and 40 pixels, respectively (raw pixel size 0.492×0.492 arcsec^2). The resulting unsharped-masked image has then been smoothed further with a Gaussian kernel of $\sigma = 2$ pixels. Contours represent the 330 MHz radio map and contour levels are the same as Figure 2. Note the extension to the south, which corresponds to a cavity in the X-ray emission that has not been seen before.

The arcsecond resolution VLA data enable us to investigate the large scale structure of the radio source. The morphology of the low frequency radio lobes clearly indicates that they are associated with the cavities present in the X-ray emission. The low frequency data also reveal the presence of an extension to the south which corresponds to an X-ray hole. We computed the age of the bubbles based on the sound speed of the surrounding gas, the buoyancy time, and the radiative age: they are all in fair agreement. Estimates of the power necessary to blow these cavities suggest that the accretion power onto the central engine has not been constant over time.

We thank the referee for constructive comments that improved the quality of the paper. GBT acknowledges support for this work from the National Aeronautics and Space Administration through Chandra Award Number GO4-5134A issued by the Chandra X-ray Observatory Center, which is operated by the Smithsonian Astrophysical Observatory for and on behalf of the National Aeronautics and Space Administration under contract NAS8-03060. GBT is also grateful for hospitality at the CNR in Bologna where a lot of this work was performed. Basic research in radio astronomy at the Naval Research Laboratory is supported by 6.1 base funding.

REFERENCES

Allen, S. W., Dunn, R. J. H., Fabian, A. C., Taylor, G. B., & Reynolds, C. S. 2006, MNRAS, 372, 21
Bîrzan, L., Rafferty, D. A., McNamara, B. R., Wise, M. W., & Nulsen, P. E. J. 2004, ApJ, 607, 800
Bennett, A. S. 1962, MmRAS, 68, 163
Burbidge, E. M. 1962, ApJ, 136, 1134
Burns, J. O., Schwendeman, E., & White, R. A. 1983, ApJ, 271, 575
Capetti, A., de Ruiter, H. R., Fanti, R., Morganti, R., Parma, P., & Ulrich, M.-H. 2000, A&A, 362, 871
Dodson, R., Edwards, p. G., Hirabayashi, H., 2006, PASJ, 58, 243
Dunn, R. J. H., & Fabian, A. C. 2004, MNRAS, 355, 862
Erickson, W. C. 1984, Journal of Astrophysics and Astronomy, 5, 55
Fabian, A. C., Sanders, J. S., Allen, S. W., Crawford, C. S., Iwasawa, K., Johnstone, R. M., Schmidt, R. W., & Taylor, G. B. 2003, MNRAS, 344, L43
Fabian, A. C., Reynolds, C. S., Taylor, G. B., & Dunn, R. J. H. 2005, MNRAS, 363, 891
Fanti, C., Fanti, R., de Ruiter, H. R., & Parma, P. 1986, A&AS, 65, 145
Feretti, L., Comoretto, G., Giovannini, G., Venturi, T., Wehrle, A. E., 1993, ApJ, 408, 446
Forman, W., et al. 2005, ApJ, 635, 894
Ge, J., & Owen, F. N. 1994, AJ, 108, 1523
Giovannini, G., Cotton, W. D., Feretti, L., Lara, L., & Venturi, T. 1998, ApJ, 493, 632
Giroletti, M., et al. 2004, ApJ, 600, 127
Giroletti, M., Giovannini, G., Taylor, G. B., Falomo, R., 2006, ApJ, 646, 801
Högbom, J. A., 1974, A&AS, 55, 179
Johnstone, R. M., Allen, S. W., Fabian, A. C., & Sanders, J. S. 2002, MNRAS, 336, 299
Lind, K. R.; Blandford, R. D., 1985, ApJ, 295, L358
Martel, A. R., et al. 1999, ApJS, 122, 81
Minkowski, R. 1961, AJ, 66, 558
Owen, F. N., Eilek, J. A., 1998, ApJ, 493, 73

Pearson, T. J., Shepherd, M. C., Taylor, G. B., & Myers, S. T. 1994, Bulletin of the American Astronomical Society, 26, 1318
Sanders, J. S., Fabian, A. C., 2006, MNRAS, 371, L65
Schwab, F. R., & Cotton, W. D. 1983, AJ, 88, 688
Taylor, G. B. 1996, ApJ, 470, 394
Taylor, G. B., & Vermeulen, R. C. 1997, ApJ, 485, L9
Taylor, G. B., O'Dea, C. P., Peck, A. B., & Koekemoer, A. M. 1999, ApJ, 512, L27
Wakker, B., Schwarz, U., 1988, A&A, 200, 312
Wilkinson, P. N., Polatidis, A. G., Readhead, A. C. S., Xu, W., & Pearson, T. J. 1994, ApJ, 432, L87
Zavala, R. T., Taylor, G. B., 2002, ApJ, 566, L9